PHYSICAL REVIEW B **80**, 144103 (2009)

Dynamical behavior of SeO_4 tetrahedra in protonic conductor $K_3H(SeO_4)_2$

Fumihito Shikanai,[1,*] Keisuke Tomiyasu,[2,†] Naofumi Aso,[3,‡] Susumu Ikeda,[1] and Takashi Kamiyama[1]
[1]*Institute of Materials Structure Science, High Energy Accelerator Research Organization, Tsukuba, Ibaraki 305-0801, Japan*
[2]*Institute for Materials Research, Tohoku University, Sendai 980-8577, Japan*
[3]*Neutron Science Laboratory, Institute for Solid State Physics, University of Tokyo, Tokai, Ibaraki 319-1106, Japan*
(Received 20 May 2009; revised manuscript received 26 July 2009; published 7 October 2009)

Neutron powder diffraction and inelastic neutron scattering experiments were performed to clarify the mechanism of phase transition and protonic conductivity of $K_3H(SeO_4)_2$. A rotational SeO_4 tetrahedra mode at the zone boundary *L*-point accounts for the symmetrical change in space group from $R\bar{3}m$ to $C2/c$. No significantly anomaly was observed in the transversal acoustic and under-damped optical modes, while a broad spectrum was observed around 0 meV at the *L*-point above T_C. The spectrum depends on the temperature and the dependence is represented by the soft mode due to an over-damped phonon both *Q* and energy space. The rotational mode of tetrahedra drives the improper ferroelastic phase transition.

DOI: 10.1103/PhysRevB.80.144103 PACS number(s): 66.30.H−, 61.05.F−, 77.84.Fa

I. INTRODUCTION

Certain hydrogen-bonded dielectric materials, such as electrolytes for fuel cells that function above the boiling temperature of water, have attracted much attention. These materials undergo a phase transition in the high-temperature region above 350 K and show high-electric conductivities that are over 100 times higher at room temperature.[1] The proton conduction mechanism of those hydrogen-bonded materials is expected to apply to next-generation electrolytes, and has been discussed from various scientific perspectives; including statical investigations such as dielectric, thermal, and structural studies,[2–7] dynamical investigations such as optical studies,[8–10] nuclear magnetic resonance (NMR),[11,12] quasielastic neutron scattering (QENS), inelastic neutron scattering (INS),[13–16] and theoretical studies.[17,18] On the other hand, these materials have been investigated for years as hydrogen-bonded dielectrics from the viewpoint of the phase transition mechanism. Most of them show ferroelasticity at room-temperature phases.[19,20] In addition to the high-temperature phase transition, many studies have investigated the low-temperature phase transition, which shows marked isotope effects on transition temperature due to deuteration.[21–32]

$K_3H(SeO_4)_2$ (TKHSe) undergoes a first-order phase transition at 390 K (T_C) and 385 K during warming and cooling, respectively.[20] The material shows remarkably high-electrical conductivities (10^{-3} S/cm) above T_C (phase I) and is ferroelastic below T_C (phase II).[2] The ferroelastic phase transition has been reported as an improper type.[19] The crystal belongs to the monoclinic system with the space group $C2/c$ in phase II and to the trigonal system with the space group $R\bar{3}m$ in phase I.

The crystal structure in phase II is characterized by isolated SeO_4-H-SeO_4 dimers including a hydrogen bond.[31,32] No hydrogen bond exists between dimers. The dimers form a layered structure parallel to the monoclinic *bc* plane. Six SeO_4 tetrahedra form a deformed hexagon inside the layer space by aligning with the pseudo $\bar{3}$ axis that is perpendicular to the *bc* plane. In phase I, a SeO_4 tetrahedron is linked to one of the nearest three equivalent SeO_4 tetrahedra by disconnection and reconstruction of the hydrogen bonds. The oxygen atoms are distributed anharmonically and occupy triangularly distributed positions with a probability of 1/3 in phase I.[4,6] This situation is closely linked to the mechanism of proton transfer at the inside of the layer. Many models are based on proton transfer within the layer accompanied by reconstruction of the hydrogen bond.[4,5,13,17,18] In reality, the crystal shows the highest conductivities in a direction parallel to the *bc* plane. However, although the deformation or rotation of tetrahedra plays an important role in these models, little evidence has been reported. Therefore, the relation between the ferroelastic phase transition and the proton conducting mechanism is still unclear. Moreover, the weak isotope effect on T_C by deuteration suggests that the hydrogen makes a small contribution to the high-temperature phase transition, while a drastic phenomenon such as protonic conduction occur above T_C.

In this paper, we focus on SeO_4 tetrahedra, which are closely related to the mechanism of protonic conduction. We report the details of static structural change due to phase transitions from the results of structural analyses by neutron powder diffraction, and discuss the connection between the symmetrical and structural changes from group theoretical analyses. We also report the results of INS measurements using a single crystal to clarify the role of SeO_4 tetrahedra for protonic conduction and the ferroelastic phase transition.

II. EXPERIMENT

Neutron powder diffraction measurements were performed using a time-of-flight powder diffractometer, VEGA, installed at KENS in the High Energy Accelerator Research Organization. Powdered samples of 3.89 g, prepared from single crystals of TKHSe were enclosed in a vanadium foil cell with Ar gas, which was set into an electric furnace made from a Cu block. The data were recorded after about 40 h. at temperature of 298 and 385 K in phase II and 393 and 413 K in phase I. Rietveld analyses were performed by RIETAN 2001T modified for VEGA using data from 0.75 Å to 4.85 Å in *d* space.

INS measurements were performed using a high-energy-resolution triple-axis spectrometer (C1–1 HER) installed at

TABLE I. Atomic fractional coordinate parameters and thermal parameters, β_{ij} ($\times 10^3$ Å^{-2}) of $K_3H(SeO_4)_2$. Their standard deviations are in parentheses.

	x	y	z	Occ.	B_{eq}	β_{11}	β_{22}	β_{33}	β_{12}	β_{13}	β_{23}
Phase II ($C2/c$)											
298 K, a_m=14.9699(1) Å, b_m=5.90777(2) Å, c_m=10.1370(5) Å and β=103.6386(5)°, Z=4, R_{wp}=0.95%, R_{I}=0.43%, and S=1.23											
Se1	0.38405(5)	0.7318(2)	0.53957(8)	1.0	0.76(3)	1.01(5)	5.3(4)	1.7(1)	0.2(1)	0.17(7)	0.4(2)
K1	0.5	0.2543(6)	0.75	1.0	1.33(8)	1.2(1)	12.5(10)	3.0(3)	0	0.1(2)	0
K2	0.3028(1)	0.2376(4)	0.3480(2)	1.0	1.65(5)	2.6(1)	7.2(7)	3.8(2)	−2.2(4)	−0.3(1)	−1.7(6)
O1	0.49745(8)	0.6812(2)	0.5648(1)	1.0	1.80(5)	0.91(8)	17.1(7)	5.7(2)	0.4(2)	0.4(1)	−0.5(3)
O2	0.34244(8)	0.5131(3)	0.6015(1)	1.0	1.72(5)	2.06(9)	8.4(5)	6.5(2)	−0.5(2)	1.8(1)	2.5(3)
O3	0.34601(7)	0.7504(3)	0.3765(1)	1.0	1.87(4)	2.30(9)	19.7(5)	2.0(2)	1.8(2)	0.1(1)	1.3(4)
O4	0.37069(9)	0.9630(3)	0.6178(1)	1.0	1.79(5)	2.4(1)	6.7(5)	6.3(2)	−1.0(2)	1.1(1)	−4.6(3)
H1	0.5011(6)	0.535(1)	0.5127(8)	0.5	1.6(1)						
385 K, a_m=15.0199(2) Å, b_m=5.92317(4) Å, c_m=10.1737(1) Å and β=103.6163(8)°, Z=4, R_{wp}=1.50%, R_{I}=0.87%, and S=1.80											
Se1	0.38465(1)	0.7317(4)	0.5397(2)	1.0	1.33(5)	1.70(9)	9.8(7)	2.7(2)	0.2(3)	0.1(1)	−0.3(4)
K1	0.5	0.250(1)	0.75	1.0	2.3(1)	2.7(3)	17.7(20)	4.8(6)	0	0.0(4)	0
K2	0.3013(2)	0.2402(8)	0.3469(4)	1.0	2.7(1)	3.8(2)	9.4(12)	7.3(5)	−1.2(7)	−1.5(3)	1.2(12)
O1	0.4961(2)	0.6830(4)	0.5656(3)	1.0	3.1(1)	2.1(1)	26.4(16)	9.5(5)	1.9(4)	1.0(2)	0.4(5)
O2	0.3437(2)	0.5133(5)	0.6021(3)	1.0	2.54(9)	3.0(2)	15.5(9)	8.2(4)	−1.5(4)	2.2(2)	4.0(5)
O3	0.3467(1)	0.7492(5)	0.3786(2)	1.0	2.97(8)	3.9(2)	26.9(10)	4.0(3)	1.5(5)	0.1(2)	−0.0(8)
O4	0.3704(2)	0.9592(5)	0.6177(3)	1.0	2.98(10)	4.1(2)	9.1(10)	10.7(5)	−1.7(4)	1.7(3)	−6.4(6)
H1	0.501(1)	0.543(2)	0.510(2)	0.5	2.9(3)						
Phase I ($R\bar{3}m$)											
393 K, a_t=8.0262(1) Å and α=43.167(7)°, Z=1. R_{wp}=1.55%, R_{I}=1.88%, and S=1.68											
Se1	0.40941(4)	x	x	1.0	3.0(2)	28.9(4)	β_{11}	β_{11}	−11.9(2)	β_{12}	β_{12}
K1	0	0	0	1.0	3.7(2)	37.2(10)	β_{11}	β_{11}	−15.7(5)	β_{12}	β_{12}
K2	0.19874(9)	x	x	1.0	4.2(1)	42.0(8)	β_{11}	β_{11}	−17.7(4)	β_{12}	β_{12}
O1	0.2551(6)	0.3742(3)	y	1/3	3.89(9)						
O21	0.2744(6)	x	0.710(1)	1/3	6.0(2)						
O22	0.3156(6)	0.2516(4)	0.7401(4)	1/3	2.46(8)						
H1	0.064(2)	0.455(1)	y	1/6	6.3(3)						
413 K, a_t=8.0297(1) Å and α=43.194(7)°. Z=1. R_{wp}=1.42%, R_{I}=1.97%, and S=1.77											
Se1	0.40948(4)	x	x	1.0	3.17(9)	30.9(5)	β_{11}	β_{11}	−12.8(3)	β_{12}	β_{12}
K1	0	0	0	1.0	4.0(2)	39.8(10)	β_{11}	β_{11}	−16.8(5)	β_{12}	β_{12}
K2	0.19960(9)	x	x	1.0	4.5(1)	45.1(7)	β_{11}	β_{11}	−19.0(4)	β_{12}	β_{12}
O1	0.2547(6)	0.3746(3)	y	1/3	3.9(1)						
O21	0.2736(5)	x	0.7115(9)	1/3	6.1(2)						
O22	0.3177(6)	0.2516(4)	0.7392(3)	1/3	2.80(8)						
H1	0.076(2)	0.4491(9)	y	1/6	6.7(3)						

the JRR-3M reactor of the Japan Atomic Energy Agency. A single crystal, $2\times1\times1$ cm^3 in size, was prepared for INS measurements and oriented with the crystallographic trigonal c_t axis perpendicular to the scattering plane. Energy scans were performed to measure phonon dispersion on the reciprocal space from 0 2 0 to 0.5 2 0 and from 0 1.5 0 to 0 1.9 0 with an energy transfer range from −10 to −0.4 meV, and the incident momentum vector k_{i} was fixed at 1.555 Å^{-1}. Measurements were performed using a cryostat for high temperatures at 413 and 388 K. Additional INS measurements were performed at the zone boundary L-point (0.5 2 0) with an energy transfer range from −2 to 4 meV at 435, 415, and 386 K. The final momentum vector k_{f} was fixed at 1.555 Å^{-1}. The energy resolution was about 0.14 meV under a horizontal collimation of Guide-Be-Open-Sample-80′ −80′. In addition, to obtain possible high resolution within the scattering conditions, and to reduct the half lambda, an energy scan at the L-point from −0.2 to 0.2 meV was performed to measure the broad spectrum around 0 meV under a collimation of Guide-Be-20′ Sample-40′-Be-40′ The final momentum vector k_{f} was fixed at 1.39 Å^{-1}. The energy resolution was estimated as 88(3) μeV from the full width at

TABLE II. Interatomic distances (Å) and bond angles (deg) of $K_3H(SeO_4)_2$. Symmetry code: (*a*) $-x$, $-y$, $-z$, (*b*) $-x$, $+y$, $-z+1/2$, (*c*) $-x+1/2$, $-y+1/2$, $-z$, (*d*) $x+1$, y, z, (*e*) $-x$, $-y-1$, $-z$ for phase II, and (*A*) $-z$, $-y$, $-x$, (*B*) y, z, x, (*C*) x, y, z, (*D*) z, x, y, (*E*) $-y$, $-z$, $-x$, (*F*) $-y$, $-x$, $-z$, (*G*) x, $y+1$, z, (*H*) $x+1$, $y+1$, $z+1$, (*I*) $x+1$, y, z, for phase I.

	298 K	385 K	393 K	413 K
		Hydrogen bond		
O1^{A}-O1^{a,B}	2.522(2)	2.562(6)	2.601(10)	2.595(9)
O1^{A}-H1^{A}	1.021(7)	1.02(2)	0.94(2)	0.89(2)
H1^{A}···O1^{a,B}	1.501(7)	1.55(2)	1.63(3)	1.74(1)
H1^{A}···H1^{a,B}	0.48(1)	0.55(2)	0.86(4)	0.94(3)
O1^{A}-H1^{A}···O1^{a,B}	177.9(5)	174.5(7)	160.9(9)	160.7(9)
		Other O-O distances		
O1^{A}···O1^{b,C}	3.738(2)	3.727(5)	3.814(10)	3.822(9)
O2^{c}(O22^{D})···O3(O22^{E})	3.203(2)	3.234(3)	3.19(1)	3.193(8)
O2^{c}(O22^{D})···O4(O21^{F})	3.434(1)	3.461(3)	3.43(2)	3.43(1)
O3^{c}(O22^{B})···O4(*O*21^{F})	3.494(2)	3.495(3)	3.56(1)	3.57(1)
		SeO_4 tetrahedron		
Sel-O1^{B}	1.683(1)	1.657(3)	1.683(7)	1.683(7)
-O2(O22^{D})	1.624(2)	1.624(3)	1.670(6)	1.668(6)
-O3(O22^{B})	1.620(1)	1.607(2)	1.670(6)	1.668(6)
-O4(O21)	1.615(2)	1.603(4)	1.502(12)	1.511(9)
O1^{B}-Sel-O2(O22^{D})	105.4(1)	105.1(2)	101.8(2)	101.6(2)
-O3(O22^{B})	105.4(1)	106.0(2)	104.5(2)	104.5(2)
-O4(O21)	108.3(1)	108.4(2)	112.4(2)	112.4(2)
O2(O22^{D})-Sel-O3(O22^{B})	111.9(1)	112.0(2)	120.2(2)	120.6(2)
-O4(O21)	112.4(1)	111.6(2)	108.3(2)	108.5(2)
O3(O22^{B})-Sel-O4(O21)	112.9(1)	113.2(2)	108.5(2)	108.0(2)
		Lattice		
K1^{c}-K1^{G}	7.98907(5)	8.01796(7)	8.0262(1)	8.0297(2)
-K1^{a}	8.047(2)	8.073(4)		
-K1^{d,H} (c_h)	21.8229(1)	21.8977(2)	21.7984(5)	21.8049(4)
K1^{c}-K2	4.405(1)	4.399(2)	4.333(2)	4.352(2)
K1^{G}-K1^{c}-K1^{a,I}	42.719(1)	42.908(1)	43.167(7)	43.194(7)
K1^{a}-K1^{c}-K1^{e}	43.073(1)	43.044(1)		
K1^{G}-K1^{c}-K2	25.42(3)	25.44(4)	25.14(2)	25.15(2)
K1^{a}-K1^{c}-K2	25.37(3)	25.49(4)		

half maximum (FWHM) of incoherent scattering of hydrogen. The phase transition temperature was 385 K because the transition occurred during cooling.

III. RESULTS AND DISCUSSIONS

A. Crystal structure

The results of Rietveld refinement, atomic fractional, and thermal parameters obtained in phases II and I, are listed in Table I. Interatomic distances and bond angles with estimated standard deviations are shown in Table II. Structural analysis of phase I was performed using a split atom model grounded on atomic distributions from Fourier maps. The occupancies of each oxygen atom in phase I are 1/3, and that of protons is 1/6, as shown in Table I. This model corresponds to the rotational tetrahedra model and agrees best with the diffraction pattern compared to other models (the proton split and deformation tetrahedra models). Figure 1 shows the Fourier maps of scattering density at 413 K sliced at the oxygen atom's positions on (111) parallel to the layer [Fig. 1(a)], and $(11\bar{2})$ perpendicular to the layer [Fig. 1(b)]. [These cutting planes are shown in Fig. 2(b)] As shown in Fig. 1(a), the oxygen atom O1 is distributed triangularly with respect to the direction of hydrogen bonds on the layer. The

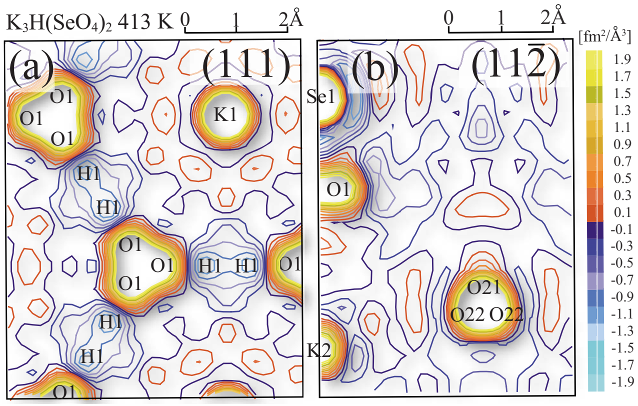

FIG. 1. (Color online) Fourier maps of $K_3H(SeO_4)_2$ at 413 K in phase I. (a) (111). (b) $(11\bar{2})$.

O1-O1 distance is 2.595(9) Å at 413 K in phase I, as shown in Table II. The other oxygen atom, O2, is also distributed triangularly, as shown in Fig. 1(b). The distribution was expressed as two kinds of oxygen atoms, O21 and O22, with occupancies of 1/3. These oxygen distributions contrast with those of K1, K2, and Se1, which are spherical explained by a harmonic vibration. A proton is in the disordered state between two oxygen atoms, as in phase II, however, the direction of the hydrogen bond cannot be determined because of the three equivalent positions, as shown in Fig. 1(a). Similar Fourier maps showing proton disorder have been reported on $Rb_3H(SeO_4)_2$ (TRHSe) in phase I[6], $K_3H(SO_4)_2$ (TKHS),[22,24] $K_3D(SO_4)_2$,[23] and TKHSe[32] in phase II. The H-H distance is 0.94(3) Å at 413 K and decreases as the O-O distance with decreasing temperature, as listed in Table II. Thus, the proton is in the disordered state in both phases I and II showing that both phases are the palaelectric phase. In addition, this suggests that the phase transition is not order-disorder type, because no permanent dipole, which interacts with each other is defined for the ferroelastic phase transition. This indicates that the oxygen atoms vibrate anharmonically in phase I, although the distributions are also explained as the order-disorder of tetrahedra.

Crystal structures at 298 K in phase II and at 413 K in phase I are illustrated in Figs. 2(a) and 2(b), respectively. Figure 2(b) shows that the potassium atom K1 constructs a trigonal lattice, and two K2 atoms and two SeO_4 tetrahedra are lined up on the $\bar{3}$ axis. The tetrahedra distribute around the mean structure position rotationally with the position of the Se atom at the center. Proton are distributed around each face-centered position of the lattice with a probability of 1/6. On the other hand, as shown in Fig. 2(a), one of the K-K distances corresponding to the lattice constant in phase I decreases from 8.0297(1) to 7.98907(5) Å, while the other two increase equivalently to 8.047(2) Å in phase II. No hydrogen bond exists between two tetrahedra in the neighboring b_t direction (c_m in phase II), which is one of the equivalent three directions in phase I. This shows that slight deformation of the lattice by about 5/100 Å determines the hydrogen bond arrangements in phase II, and the situations are closely related to the ferroelasticity in phase II.

Figures 2(c) and 2(d) present the arrangements of SeO_4 tetrahedra at 298 and 413 K, respectively. In phase I, supposing that the oxygen atoms are allocated at the points painted red [Fig. 2(d)], the interatomic distances of O-O and the appearance of tetrahedra arrangements are congruent with those in phase II [Fig. 2(c)]. The results suggest that a hydrogen bond exists between two tetrahedra forming a dimer even in phase I, and such local structures distribute with the probability of 1/3.

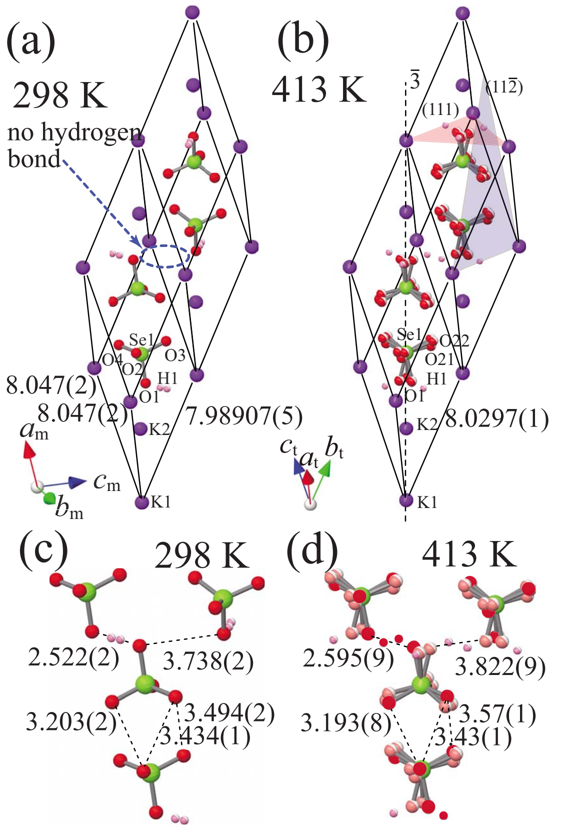

FIG. 2. (Color online) Crystal structure of $K_3H(SeO_4)_2$. The numbers in the figures are inter-atomic distances (Å) with their standard deviations in the parentheses. (a) At 298 K in phase II. The lattice is taken to be a pseudo rhombohedral cell. (b) At 413 K in phase I. (c) Arrangement of SeO_4 tetrahedra at 298 K. (d) Arrangement of SeO_4 tetrahedra at 413 K.

B. Symmetrical and structural changes accompanied by phase transition

Here, we revisit the details of structural change, this time from the viewpoint of symmetrical change from $R\bar{3}m$ to $C2/c$. When an atomic density function $\rho_0(\mathbf{r})$ changes to $\rho_0(\mathbf{r})+\Delta\rho(\mathbf{r})$ accompanying a phase transition, the $\Delta\rho(\mathbf{r})$ is invariant for symmetry operations g_i belonging to the low-symmetry phase's group, $g_i\Delta\rho(\mathbf{r})=\Delta\rho(\mathbf{r})$, and can be considered an order parameter. The space group is expressed as a semidirect product (denoted as $\wedge$) of a translational group and Γ-point group, because these groups are nonexchangeable in general. The irreducible representations of the translational group are identical to $\exp[i\boldsymbol{k}\cdot\boldsymbol{r}_n]$, where $\boldsymbol{r}_n$ consists of discrete translational vectors based on the lattice vectors. The relationships between the lattice in phase I and II are as

TABLE III. Character table at L point of $R\bar{3}m$ and maximal subgroups of each irreducible representation.

	E	C_2'	I	σ_d	$\{E\|b_t\}$	$\{C_2'\|b_t\}$	$\{I\|b_t\}$	$\{\sigma_d\|b_t\}$	
L_1	1	1	1	1	−1	−1	−1	−1	$C2/m$
L_2	1	1	−1	−1	−1	−1	1	1	$C2/c$
L_3	1	−1	1	−1	−1	1	−1	1	$C2/c$
L_4	1	−1	−1	1	−1	1	1	−1	$C2/m$

follows: $a_p=(a_m-b_m)/2=c_t$, $b_p=(a_m+b_m)/2=a_t$, and $c_p=c_m=-a_t+2b_t-c_t$, where, the subscript of p represents the primitive unit cell. The translational group in phase II, $t(\boldsymbol{k})$, is identical to $\exp[i\boldsymbol{k}\cdot(la_p+mb_p+nc_p)]$ (l, m, n: integer). Using the relationship between the axes, the translational group in phase I, $T(\boldsymbol{k})$, is shown as

$$T(\boldsymbol{k}) = t(\boldsymbol{k}) \times e^{-imkb_t} = t(\boldsymbol{k}) \otimes \{E|b_t\}. \tag{1}$$

Equation (1) shows that the lattice interval in the direction of b_t in phase II is twice of that in phase I. In fact, many superlattice reflections with an index of $h\ k/2\ l$ are observed in phase II[6]. Hence, the space group $R\bar{3}m$ is transformed using Eq. (1).

$$R\bar{3}m = T(\boldsymbol{k}) \wedge \{\Gamma-\text{point}\} = t(\boldsymbol{k}) \otimes C_3 \wedge \{L-\text{point}\}. \tag{2}$$

The C_3 term replaces the groups trigonal axes.

Table III shows the character table for the L-point. Symmetry elements, C_2', I, and σ_d, are illustrated in Fig. 3(c). The dihedral mirror plane, σ_d, includes the b_t axis. The twofold axis, C_2', goes through the center of the unit cell, and is perpendicular to the σ_d. The inversion, I, is at the intersection of σ_d and C_2'. As shown in Table III, the space group of phase II, $C2/c$, is the maximal sub group of the L-point of $R\bar{3}m$, and representations L_2 and L_3 relate to the change from $R\bar{3}m$ to $C2/c$. Figure 3 shows the representative results obtained using the projection operator for arbitrary atomic displacements, which are parallel and perpendicular to the Se-O bonds. As shown in Fig. 3(c), the stretching displacements of Se-O cancel in the cases of both L_2 and L_3. This result demonstrates that the stretching mode of Se-O is independent of symmetrical change. On the other hand, rotational displacements are derived from vertical components of oxygen displacements, as shown in Figs. 3(a), 3(b), 3(d), and 3(e). The rotational axes correspond to one of the Se-O bonds. As shown in the figures, the L_2 modes correspond to rotational displacements in the opposite direction, while the L_3 modes correspond to those in the same direction. Figure 3(f) exhibits the composition of L_{3b} and L_{3c}. The rotational axes incline to the bisector of the O-Se-O angles. The tetrahedra tilt to the hydrogen bond and the rotational displacements are identical to those in phase II shown in Figs. 2(c) and 2(d). As mentioned above, a slight deformation of the potassium lattice determines the hydrogen bond orientation in phase II, and an alternate rotational displacement of SeO_4 tetrahedra, explained as a zone boundary phonon mode, corresponds to the crystal structure in phase II.

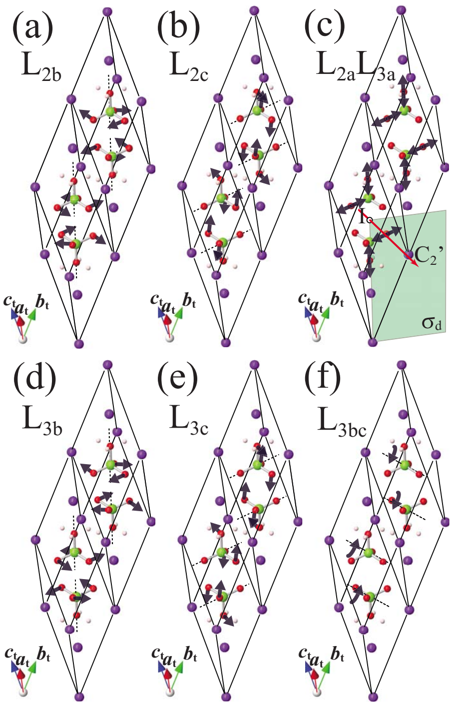

FIG. 3. (Color online) Various atomic displacements that belong to a group of the zone boundary L-point. (a), (b) L_2 mode. (c) Stretching mode of Se-O. (d), (e), (f) L_3 mode.

C. Inelastic neutron scattering

Figure 4(a)–4(e) show INS spectra at 413 and 388 K in phase I, from Γ-point 0 2 0 to L-point 0.5 2 0, with an energy transfer range from −10 meV to −0.4 meV. As shown in Fig. 4(a), five optical modes were observed at Γ-point; OP1: −1.4(1) meV [11.4(9) cm^{-1}], OP2: −4.3(1) meV [34.9(8) cm^{-1}], OP3: −6.6(1) meV [53(1) cm^{-1}], OP4: −8.1(2) meV [66(1) cm^{-1}] and OP5: −9.4(3) meV [76(2) cm^{-1}]. Detailed assignments for $Na_3H(SO_4)_2$, TKHS and $Rb_3H(SO_4)_2$ (TRHS) using the infrared (IR) absorption, Raman scattering, and INS have been reported,[30] as well as those for TRHSe using INS and Fourier transform infrared (FTIR) spectroscopy.[16] In comparison with those results, OP3 and 5 are assigned as the lattice modes of potassium reported as 53 cm^{-1} and 77 cm^{-1} in TKHS, respectively.[30] Although OP4 has not been mentioned, it is naturally expected that the mode is a similar lattice mode. OP2 has been observed at 57 cm^{-1} and 44 cm^{-1} for TKHS and TRHS, respectively,[30] and is assigned as ν-OH. In addition, the mode is suggested either weak coupling with the underlying phonon density of states or a nonequivalent $(SO_4HSO_4)^{-3}$ species form the asymmetric profile of the mode. The mode has also been observed at 37.8 cm^{-1} for TRHSe.[16] The intensity of OP1 in Fig. 4(a)–4(e) is extremely weak; however, it is observed at 2.0(2), 1.8(2), and 1.8(2) meV at 435, 415, and 386 K, respectively [Fig. 4(f)]. OP1 and 2 are considered to be the L_2 modes mentioned in Figs. 3(a) and 3(b). It is expected that the energy of L_2 modes is higher than that of the L_3 mode, although the energies of both modes are close, because the L_2 modes have a node in the unit cell. Furthermore, as in the presented result, the modes have been ob-

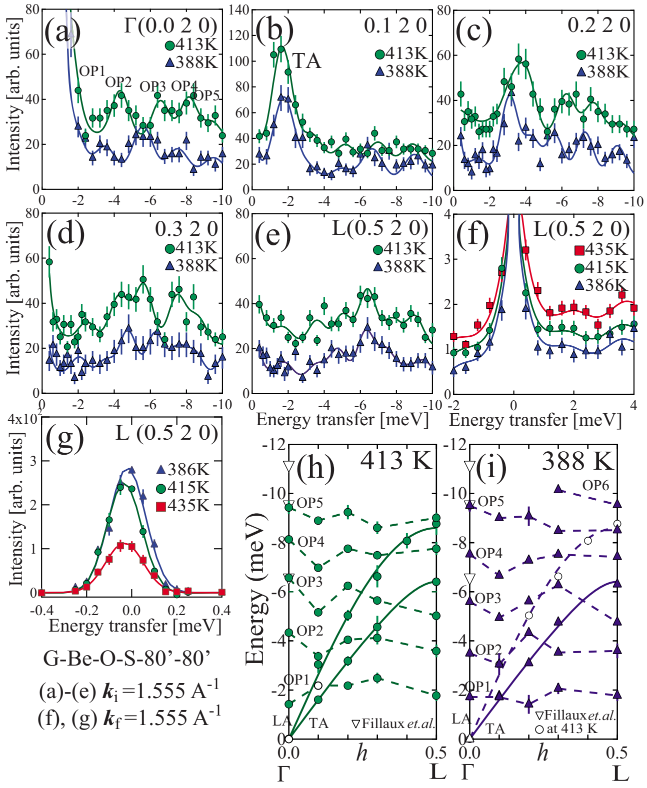

FIG. 4. (Color online) Inelastic neutron scattering spectra of $K_3H(SeO_4)_2$ in phase I. (a)-(e) Energy transfer range of -10 meV to -0.4 meV. (f), (g) Energy transfer range of -2 meV to 4 meV at L-point. (h), (i) Phonon dispersion curves obtained from INS spectra. The open characters were fixed. Data denoted by ∇'s are those of TKHS at 20 K from Reference.[30]

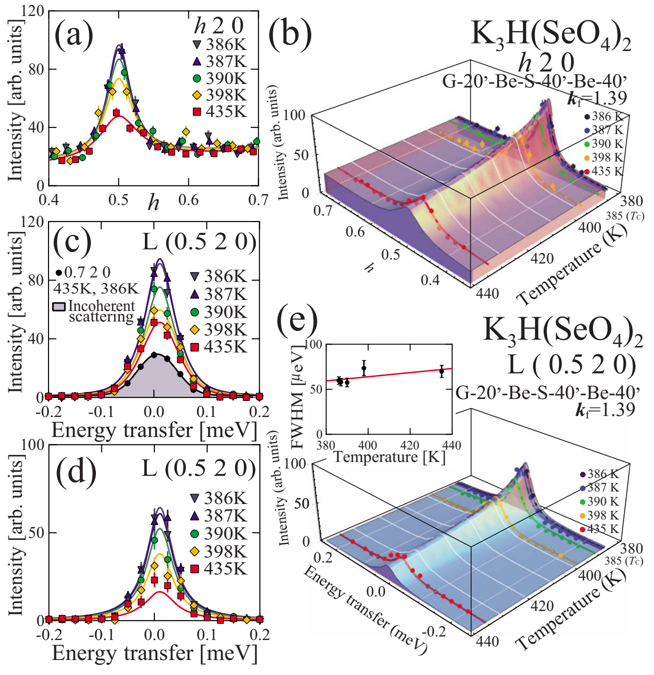

FIG. 5. (Color online) (a),(b) Temperature and the h dependence of elastic scattering. Temperature dependence of inelastic neutron scattering spectra at L-point of $K_3H(SeO_4)_2$ in phase I. (c) Raw data (d),(e) Data with incoherent scattering subtracted.

served by INS measurements in both reports. The L_2 representation is compatible with the A_{1u} and E_u representations at the Γ-point. The A_{1u} mode is compatible with the L_{2b} and active only in hyper-Raman scattering, and the E_u mode is compatible with the L_{2c} and active in IR and hyper-Raman scattering optically. However, the observation must be difficult because of the low frequency. These excitations in low-energy region are open to discussion.

A large peak around -1.6 meV in Fig. 4(b) corresponds to the transversal acoustic (TA) mode. The mode shifts to 6.4(1) meV across the optical modes, as shown in Figs. 4(a)–4(e). Figures 4(h) and 4(i) are phonon dispersion curves at 413 and 388 K, respectively. The longitudinal acoustic (LA) mode was determined from the other data from 0 1.5 0 to 0 1.9 0 at 413 K. The LA mode shifts to 8.8(4) meV and connects with OP5 at the L point, as shown in Fig. 4(h); therefore, OP5 is assigned as the longitudinal optical (LO) mode of the lattice, and OP4 and 3 are transversal ones (TO). The velocity of LA and TA at 413 K were estimated from each slope in the vicinity of the Γ point using $2\pi a^* = 1.26$ Å^{-1}, as 3130(132) and 1930(78) m/s, respectively, and that of TA at 388 K is 1909(15) m/s. The elastic stiffness, $c^*=\rho v^2$, were obtained as $c^*_{\mathrm{LA}}=3.0(8)\times 10^{10}$ Pa and $c^*_{\mathrm{TA}}=1.1(3)\times 10^{10}$ Pa; here $\rho=3.05$ g(cm)$^{-3}$.

Because of overlap between peaks and poor statistics, the details of dispersion curves in Figs. 4(h) and 4(i) (the curvature, the mode anticrossing, *etc.*) are unclear in this result. However, it illustrates some intrinsic points regarding the phase transition. As shown in Figs. 4(b), 4(h), and 4(i), no significant anomaly is observed in the TA mode in the vicinity of the Γ point at T_C, which closely relates to the ferroelastic phase transition. This shows that the phase transition is independent of the softening of the TA mode. Moreover, no soft optical mode was observed at the other Q space from 0 2 0 to 0.5 2 0. On the other hand, as shown in Fig. 4(g), a broad peak was observed around 0 meV above T_C. The spectrum increases sharply with the decreasing temperature. The result is close to the spectrum of over-damped phonons on $CsPbCl_3$ due to the M_3 mode (the tilts of $PbCl_6$ octahedra).[33]

Figure 5(a) shows the temperature dependence of elastic scattering spectra obtained by an h scan from 0.4 2 0 to 0.7 2 0. It shows that the broad peak around 0 meV shown in Fig. 4(g) is observed only at the L point, and therefore, the spectra are caused by coherent scattering having the same symmetry of rotational SeO_4 tetrahedra mentioned above. The detailed energy transfer is shown in Fig. 5(c). As described in the figure, the spectrum includes incoherent scattering by hydrogen illustrated as shaded spectrum. The incoherent scattering spectrum (spectrum at 0.7 2 0) corresponds to the background in Fig. 5(a) and is independent of temperature. The energy resolution was obtained from the FWHM of the spectrum as 88(3) μeV. Figure 5(d) shows the temperature dependence of the spectrum with incoherent scattering subtracted. The spectrum increases with decreasing temperature, and the peak shape is narrower than the resolution. To analyze the data in Figs. 5(a) and 5(d), the following equation formulated for the neutron scattering cross section by over-damped phonons[34] was used.

$$\left(\frac{d^2\sigma}{d\Omega d\omega}\right)_{dp} \cong N\frac{k'}{k}|F_{\text{ph}}(\mathbf{K})|^2\frac{\hbar kT}{\pi}\frac{1}{\alpha(T-T_0)+a\Delta q^2} \times \frac{\omega_1^2/\Gamma'}{\omega^2+(\omega_1^2/\Gamma')^2}, \qquad (3)$$

where, $F_{\text{ph}}(\mathbf{K})$ is the dynamic structure factor. Equation (3) takes the form of the Lorentz function for both Δq and ω, and is roughly proportional to $T/(T-T_0)$. In this analysis, Eq. (3) was simplified as $AT\gamma\{(T-T_0+B\Delta q^2)(E^2+\gamma^2)\}^{-1}$ with the four parameters A, B, T_0, and γ. The results of fitting, substituting $E=0$ and $\Delta q=0$, for the fitting function are illustrated in Figs. 5(b) and 5(e), respectively, and those at each temperature are shown as the lines in Figs. 5(a) and 5(d). The extrapolated Curie temperature T_0 was 368(2) K. The parameter γ was assumed to be a linear function of T obtained from fitting at each temperature using a normal Lorentz function, as shown in the inset of Fig. 5(e). The FWHM of the spectrum, 2γ, depends slightly on the temperature and is obtained as 60(4) and 70(6) μeV at 386 and 435 K, respectively. This energy range corresponds to 14(1) to 17(1) GHz and gives a lifetime of $7.1(4)\times10^{-11}$ to $5.9(4)\times10^{-11}$ s. Although the lifetimes are expected to be a little longer than this result because of the resolution, these time scale agree with the stationary time of the conducting protons, $9.0(8)\times10^{-11}$ s at 388 K and $4.9(3)\times10^{-11}$ s at 433 K, obtained from QENS.[14] Here, the QENS spectrum represents incoherent scattering due to the large incoherent scattering length of protons corresponding to the shaded spectrum in Fig. 5(c), in contrast to the coherent one discussed above. Thus, it is demonstrated that an over-damped rotational mode of SeO$_4$ tetrahedra with the lifetime about 10^{-10} s drives the improper ferroelastic phase transition.

IV. SUMMARY

In this study, we showed statical and dynamical details of SeO$_4$ tetrahedra in the protonic conductor TKHSe thorough the structural analysis and inelastic neutron scattering. The crystal structure in phase I shows the rotational distribution of SeO$_4$ tetrahedra locally, which corresponds to the arrangement of dimers in phase II. The rotational mode of SeO$_4$ tetrahedra L_3 meets the requirements for the symmetrical change from $R\bar{3}m$ to $C2/c$. No significant anomaly is observed in the TA and optical under-damped modes in the vicinity of T_C, while a coherent broad spectrum around 0 meV increases at the zone boundary L point above T_C. The temperature dependence of the spectrum is represented by that of the soft mode due to an over-damped phonon. Tilted tetrahedra form hydrogen bonds and dimers locally even in phase I, and the rotational mode is over-damped by the formation of the hydrogen bonds. That is, the tetrahedra rotationally vibrate, tearing the hydrogen bond throughout in the crystal above T_C, suggesting that the phase transition temperature corresponds to the binding energy of the SeO$_4$-H-SeO$_4$ dimer. On the other hand, freezing of the rotational mode determines the hydrogen bond arrangement and lattice deformation in phase II, as shown in Fig. 2(a). These situations also play an important role for proton conductivity. The lifetime of the over-damped mode, about 10^{-10} s, agrees with the stationary time of conducting protons. This shows that proton conduction is simultaneous with the motion of the rotational mode in phase I.

In contrast to the representative hydrogen-bonded material KH$_2$PO$_4$, of which the phase transition is also an improper ferroelastic but a proper ferroelectric type,[35–37] the rotational tetrahedra mode is predominant in the high-temperature improper ferroelastic phase transition of TKHSe, which induces no ferroelectricity or antiferroelectricity in phase II. From this situation, the high-temperature phase transition of TKHSe is not order-disorder type, because no permanent dipole for the ferroelastic phase transition is defined. The present results show that the rotational tetrahedra modes are capable of being an order parameter, and a new mechanism is needed.

ACKNOWLEDGMENTS

We wish to acknowledge S. Itoh and Taku J. Sato for technical support of measurement and analysis.

---

[*] Present address: Private, 2-15-11-102 Chikuho Tsukuba, Ibaraki 300-3257, Japan.

[†] Present address: Department of Physics, Graduate School of Science, Tohoku University, Sendai 980-8578, Japan.

[‡] Present address: Faculty of Science, University of the Ryukyus, Nishihara, Okinawa 903-0213, Japan.

[1] S. M. Haile, D. A. Boysen, C. R. I. Chisholm, and R. B. Merle, Nature (London) **410**, 910 (2001).

[2] J. Hatori, Y. Matsuo, and S. Ikehata, Solid State Commun. **140**, 452 (2006).

[3] Y. Matsuo, J. Hatori, Y. Yoshida, K. Saito, and S. Ikehata, Solid State Ionics **176**, 2461 (2005).

[4] B. V. Merinov, A. I. Baranov, and L. A. Shuvalov, Sov. Phys. Crystallogr. **35**, 200 (1990).

[5] A. Bohn, R. Melzer, R. Sonntag, R. E. Lechner, G. Schuck, and K. Langer, Solid State Ionics **77**, 111 (1995).

[6] R. Melzer, T. Wessels, and M. Reehuis, Solid State Ionics **92**, 119 (1996).

[7] F. Shikanai, R. Kiyanagi, M. Yonemura, D. Sulistyanintyas, K. Iwase, T. Wuernisha, K. Mori, T. Ishigaki, S. Ikeda, and T. Kamiyama, Physica B **385-386**, 156 (2006).

[8] Y. Matsumoto, J. Phys. Soc. Jpn. **70**, 1437 (2001).

[9] A. Pawłowski and M. Połomska, Solid State Ionics **176**, 2045 (2005).

[10] A. Fedoseev, A. Svanidze, S. Kojima, and S. Lushnikov, Mater. Sci. Eng., A **442**, 224 (2006).

[11] J. Dolinšek, U. Mikac, J. E. Javoršek, G. Lahajnar, R. Blinc, and L. F. Kirpichnikova, Phys. Rev. B **58**, 8445 (1998).

[12] A. R. Lim and M. Ichikawa, J. Phys.: Condens. Matter **18**, 2173 (2006).

[13] R. E. Lechner, Solid State Ionics **145**, 167 (2001).
[14] F. Shikanai *et al.*, Ferroelectrics **347**, 74 (2007).
[15] A. Belushkin, J. Tomkinson, and L. Shuvalov, J. Phys. II **3**, 217 (1993).
[16] G. Schuc, R. E. Lechner, and K. Langer, Solid State Ionics. **176**, 731 (2005).
[17] H. Kamimura, Y. Matsuo, S. Ikehata, Y. Ito, M. Komukae, and T. Osaka, Phys. Status Solidi B **241**, 61 (2004).
[18] N. I. Pavlenko and I. V. Stasyuk, J. Chem. Phys. **114**, 4607 (2001).
[19] S. Yokota, Y. Makita, and Y. Takagi, J. Phys. Soc. Jpn. **51**, 1461 (1982).
[20] M. Endo, K. Kaneko, T. Osaka, and Y. Makita, J. Phys. Soc. Jpn. **52**, 3829 (1983).
[21] K. Gesi, J. Phys. Soc. Jpn. **50**, 3185 (1981).
[22] Y. Noda, S. Uchida, K. Kafuku, H. Kasatani, and H. Terauchi, J. Phys. Soc. Jpn. **59**, 2804 (1990).
[23] Y. Noda, H. Kasatani, Y. Watanabe, H. Terauchi, and K. Gesi, J. Phys. Soc. Jpn. **59**, 3249 (1990).
[24] Y. Noda, H. Kasatani, Y. Watanabe, and H. Terauchi, J. Phys. Soc. Jpn. **61**, 905 (1992).
[25] Y. Moritomo, Y. Tokura, N. Nagaosa, T. Suzuki, and K. Kumagai, Phys. Rev. Lett. **71**, 2833 (1993).
[26] P. Kaung, M. Kasahara, and T. Yagi, J. Phys. Soc. Jpn. **65**, 1114 (1996).
[27] K. Kohno, T. Matsuo, and M. Ichikawa, J. Korean. Phys. Soc. **32**, S393 (1998).
[28] C. Totsuji and T. Matsubara, J. Phys. Soc. Jpn. **63**, 2760 (1994).
[29] Y. Suwa, J. Yamaguchi, H. Kageshima, and S. Tsuneyuki, Mater. Sci. Eng. **98**, B79 (2001).
[30] F. Fillaux, A. Lautié, J. Tomkinson, and G. J. Kearly, Chem. Phys. **154**, 135 (1991).
[31] M. Ichikawa, S. Sato, M. Komukae, and T. Osaka, Acta Crystallogr., Sect. C: Cryst. Struct. Commun. **48**, 1569 (1992).
[32] N. Onoda-Yamamuro, O. Yamamuro, T. Matsuo, M. Ichikawa, R. M. Ibbreson, and W. I. F. David, J. Phys.: Condens. Matter **12**, 8559 (2000).
[33] Y. Fujii, S. Hoshino, Y. Yamada, and G. Shirane, Phys. Rev. B **9**, 4549 (1974).
[34] Y. Yamada, G. Shirane, and A. Linz, Phys. Rev. **177**, 848 (1969).
[35] F. Jona and G. Shirane, *Ferroelectric Crystals* (Dover, New York, 1993),.
[36] E. Litov and E. A. Uehling, Phys. Rev. B **1**, 3713 (1970).
[37] G. A. Samala, Ferroelectrics **22**, 925 (1978).